LIMNOLOGY and OCEANOGRAPHY

Winter entrainment drives the mixed layer supply of manganese in the Southern Ocean

Thapelo Ramalepe [1,2] Saumik Samanta [2] Ryan Cloete [2,a] Thomas J. Ryan-Keogh [1] Alakendra N. Roychoudhury [2*]
[1]Southern Ocean Carbon-Climate Observatory, CSIR, Cape Town, South Africa
[2]Centre for Trace Metal and Experimental Biogeochemistry (TracEx), Department of Earth Sciences, Stellenbosch University, Stellenbosch, South Africa

Abstract

Despite the subnanomolar dissolved manganese concentrations that can co-limit Southern Ocean primary production, their physical supply mechanisms during winter, for biological consumption in spring and summer have not yet been explored. During austral winter and spring 2019, two cruises were conducted in the Atlantic sector of the Southern Ocean, to determine the distribution and surface water supply mechanisms of dissolved manganese in the upper water column. The supply mechanisms were used to calculate the total flux of dissolved manganese to productive surface waters and were compared to biological consumption estimates. Mean dissolved manganese concentrations in the upper water column (< 500 m) during winter and spring were comparably low (≤ 0.34 nmol kg^{-1}; $p > 0.05$), with seasonal mixed layer reservoir sizes averaging 65.21 ± 12.93 and 21.64 ± 19.32 μmol m^{-2}, respectively. Winter entrainment contributed 89.33–99.99% (average 97.26% $\pm$ 5.28%) of the total dissolved manganese flux, while diapycnal diffusion contributed 0.52–10.58% (average 4.92% $\pm$ 5.14%), was identified as the dominant mechanisms for transporting dissolved manganese into the mixed layer in the subantarctic zone, polar frontal zone, and antarctic zone. Here, the winter physical supply rates were higher than the estimated consumption rates during spring, meeting phytoplankton biological demands. Whereas in the subtropical zone, the supply rates were lower than the consumption rates, indicating the presence of additional supply mechanisms such as coastal upwelling, which may help to meet the biological demands in this region.

Net primary production in the Southern Ocean is a major contributor to the biological carbon pump, accounting for ~ 2 Pg of carbon per year to global carbon export (Schlitzer 2002). To date, most studies have focused on iron as the primary micronutrient limiting phytoplankton net primary production (Boyd et al. 2000). Manganese (Mn), like iron, is required by phytoplankton for photosynthesis as a co-factor for the oxygen-evolving complex (Mn$_4$O$_5$Ca) found in photosystem II (Raven 1990; Twining and Baines 2013). Thus, Mn is also an important co-limiting micronutrient, but its biogeochemical cycling is much less constrained. Under iron-stressed conditions in the Southern Ocean, the efficiency of photosystem II reduces, so phytoplankton require additional Mn for their anti-oxidant superoxide dismutase, which combats the toxic effects of reactive oxygen species produced under such stressed conditions (Peers and Price 2004). Despite being the 12th most abundant metal in the Earth's crust (Wedepohl 1995), surprisingly, the concentration of dissolved Mn (defined as the material that passes through a 0.2 μm filter) in the open Southern Ocean can be limited to subnanomolar scale, reaching levels as low as < 0.05 nmol kg^{-1} (Latour et al. 2021; Balaguer et al. 2022). Consequently, alongside iron, dissolved Mn deficiency in the surface mixed layer may also contribute to limiting net primary production; and thereby, the extent and efficiency of the Southern Ocean biological carbon pump (Anugerahanti and Tagliabue 2023). Apart from iron, Mn consumption rates are

*Correspondence: roy@sun.ac.za

[a]Present address: Univ Brest, CNRS, IRD, Ifremer, LEMAR, Plouzané, France

Additional Supporting Information may be found in the online version of this article.

Author Contribution Statement: Conceptualization: TR, TJR, ANR. Data processing analysis: TR. Sample collection and chemical analysis: SS, RC. Writing – original draft preparation: TR. Writing – review and editing: TJR, ANR, SS, RC. Software: TR, TJR. Methodology: SS, RC. Funding acquisition and supervision: TJR, ANR.

further hindered by the antagonistic relationship between Mn and zinc. These metals compete for the same phytoplankton metal transporter, with zinc having comparatively higher affinity due to its higher concentrations in the Southern Ocean (Hawco et al. 2022). Such limitations in micronutrient availability restrict macronutrient consumption, ultimately making the Southern Ocean the largest high-nutrient, low-chlorophyll region in the global ocean (Bristow et al. 2017).

Various processes that act as supply mechanisms and sinks of dissolved Mn drive its biological consumption and cycling in the Southern Ocean mixed layer (Fig. 1). Dissolved Mn is primarily supplied to the mixed layer for biological consumption through physical supply mechanisms such as winter entrainment, diapycnal diffusion, lateral advection, vertical Ekman upwelling and eddies (Middag et al. 2011a; de Jong et al. 2012). The physical supplies are driven by wind and buoyancy fluxes, with their extent influenced by the relationship between the mixed layer depth (MLD) and the mangacline (i.e., the depth at which the vertical dissolved Mn concentration gradient is the greatest). Winter entrainment (wintertime deep mixing) is influenced by the deep-water dissolved Mn reservoir, which is usually dissolved Mn depleted.

As a result, when there is an upwelling of low dissolved Mn waters, the dissolved Mn-enriched surface layer may be diluted (Rigby et al. 2020). Periodically, the physical dissolved Mn supply is supplemented by additional external sources such as hydrothermal vents (Ardyna et al. 2019; Middag et al. 2011b), atmospheric inputs (Mendez et al. 2010), melting sea ice (Middag et al. 2013), continental margins (Latour et al. 2021), and resuspension from anoxic reducing sediments (Bucciarelli et al. 2001). Furthermore, particulate Mn oxides (material retained on 0.2 or 0.45 μm filters), which are thermodynamically stable in oxygenated environments, can undergo photoreduction processes in the atmosphere and the sunlit ocean surface layer, which seasonally converts them back to dissolved Mn ions (Sunda and Huntsman 1988). Remineralization by zooplankton has also emerged as a significant process influencing the availability of dissolved Mn in the upper ocean (Richon and Tagliabue 2021). This process has the potential to resupply dissolved Mn within this stratum through vertical advection, thereby supporting phytoplankton productivity (Laglera et al. 2017).

In terms of dissolved Mn sinks, in situ oxidation of Mn(II) to Mn(III) and Mn(IV) can result in variable residence
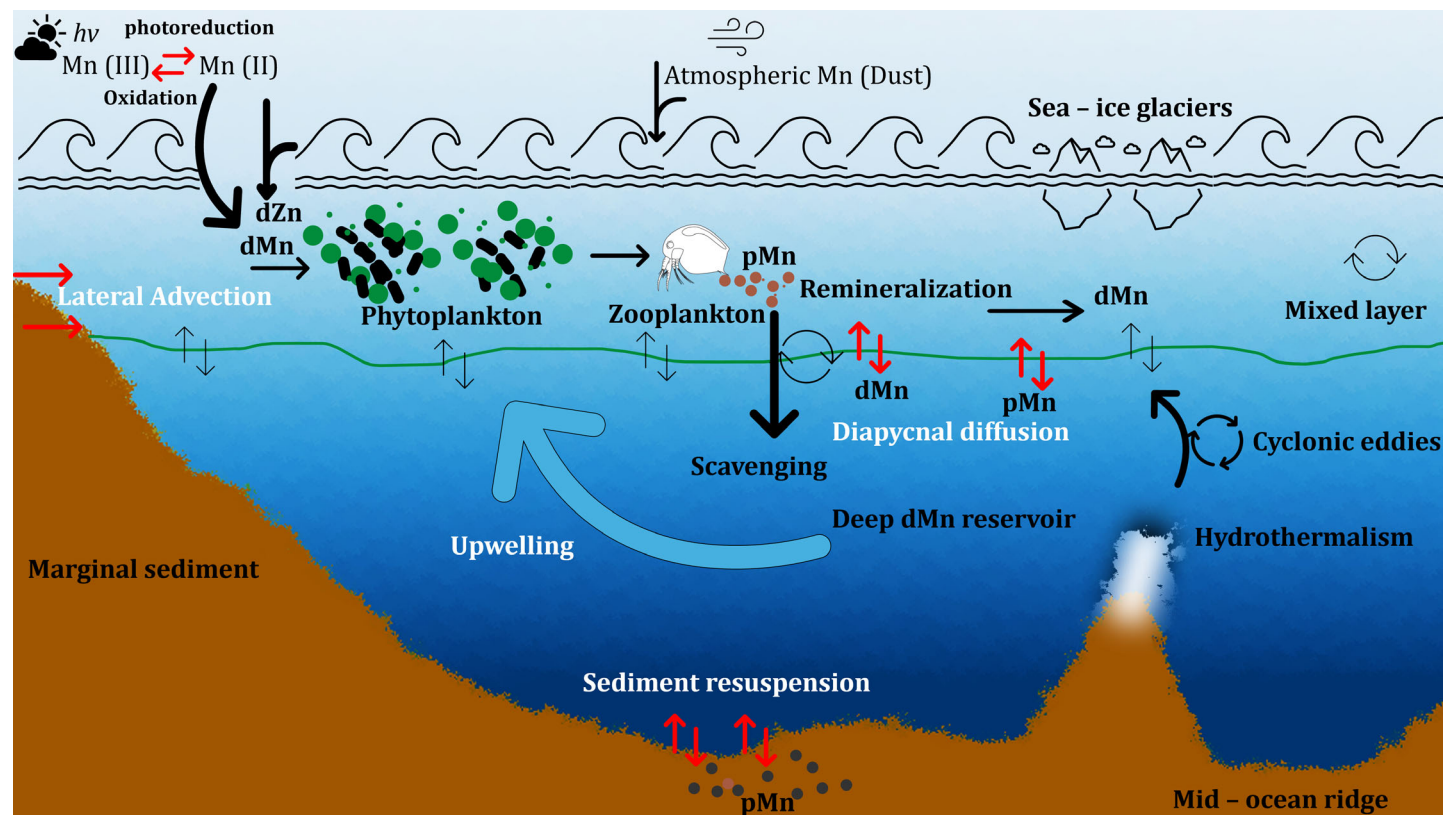

Fig. 1. Illustration of processes involved in supplying and removing dissolved manganese (dMn) and particulate manganese (pMn) within the mixed layer. Various processes are depicted, including physical mechanisms such as upwelling, diapycnal diffusion, lateral advection, and sediment resuspension. It also shows external sources such as atmospheric input, hydrothermal vents, sea ice melt, and marginal sediment, along with internal sources like remineralization, eddies, zooplankton recycling, and photoreduction. Depicted removal mechanisms include oxidation, biological consumption, and particle scavenging. In addition, it illustrates the antagonistic relationship between the biological uptake of dMn and dissolved zinc (dZn).

times between Mn species, influencing the vertical export of dissolved Mn out of the mixed layer down to the seafloor (Sunda and Huntsman 1994). These removal processes are further aided by bacterial oxidation of dissolved Mn below the sunlit layer (van Hulten et al. 2017). Whilst removal through particle scavenging is another mechanism, it is offset by the stabilization of dissolved Mn in solution by excess Mn-complexing ligands. These ligands can increase dissolved Mn residence time and, therefore, bioavailability in the mixed layer (Tebo 2019). Previous studies have indeed suggested that strong organic ligands could decrease the oxidation rates of Mn(II) to Mn(III) in anoxic environments, thereby stabilizing Mn(III) and decreasing its export out of the mixed layer (Sander and Koschinsky 2011; Oldham 2017). Quantifying the relative roles of removal processes (oxidation and particle scavenging) of dissolved Mn is based on the relative abundance of reactive particulate Mn (Mn oxyhydroxides and Mn oxides) with respect to the export flux of particulate organic carbon (Sunda and Huntsman 1998). On the other hand, quantification of biological consumption, a dissolved Mn sink, considers phytoplankton Mn : carbon ratios and estimates of daily net primary production. Mn : carbon ratios may vary for different phytoplankton species and, therefore, depend on the relative abundance of the phytoplankton species in that region (Twining and Baines 2013).

Since most of the net biological consumption in spring is reported to be sustained by winter entrainment (Rigby et al. 2020), estimates of dissolved Mn detrainment (physical proportion of the winter entrained dissolved Mn stock that is detrained during springtime mixed layer shallowing) as a sink becomes important to quantify (Tagliabue et al. 2014). Understanding such seasonal Mn dynamics may help narrow the research gap about the sensitivity of the biological carbon pump to the changing Southern Ocean physics across the mixed layer where phytoplankton growth occurs (Sallée et al. 2021). Furthermore, winter observations of trace metals in the Southern Ocean are scarce (Tagliabue et al. 2012) owing largely to inclement conditions, yet are vital for understanding phytoplankton dynamics during unfavorable growth conditions. These seasonal cycle observations help us resolve the magnitude of the dissolved Mn reservoir during the ocean reset state, which plays a critical role in shaping the nutrient budget for springtime biological uptake. On the other hand, spring is an important season for biological uptake and detrainment due to the shoaling of the mixed layer to a depth shallower than the critical depth (depth at which photosynthesis rate is equal to that of respiration), relieving light limitation (Sverdrup 1953). Our goal here is to provide insight into the winter-to-spring distribution of dissolved Mn from the Atlantic sector of the Southern Ocean during the Southern oCean seaAonaL Experiment (SCALE) 2019 cruises. The observations are used to quantify the physical supply mechanisms in winter that set the stock potentially available for biological consumption, offset by the total supply and spring mixed layer reservoir size.

Materials and methods

Sample collection and subsampling

Seawater samples were collected on board RV *SA Agulhas II* during the 2019 SCALE winter (July 18–August 12, 2019) and spring (October 12–November 20, 2019) cruises. The SCALE voyages followed approximately the GEOTRACES GIPY04 transect between Cape Town (South Africa) and the marginal ice zone in the Atlantic sector of the Southern Ocean (Fig. 2). Seawater samples were collected at various depths in 24×12-liter Teflon® coated GoFlo bottles housed on a GEOTRACES-compliant CTD rosette connected by Kevlar® cable on a clean winch. The stations spanned multiple oceanographic fronts, allowing observations in different biogeochemical zones of the Southern Ocean (Fig. 2; Supporting Information Table ST1). In winter, only 8 of the 10 planned stations could be sampled due to inclement weather (whereas spring had 10). Sampling and subsampling for dissolved trace metal samples from the GoFlo bottles were conducted following the trace metal clean protocols as per the GEOTRACES cookbook (Cutter et al. 2017) inside a class 100 clean container laboratory fitted with a class 10 laminar flow hood, as described in Cloete et al. (2021). Briefly, duplicate seawater samples for dissolved trace metals were filtered through a 0.2 μm filter (Acropak® 500 Supor Membrane) into pre-cleaned 125 mL low-density polyethylene bottles under slight nitrogen gas (0.5 bar, 99.9999% N_2; BIP Technology) overpressure. Each sample was acidified to a pH of 1.7 inside the laminar flow hood, by adding 250 μL hydrochloric acid (30% Ultrapur® HCl; Merck) and double bagged for storage at room temperature until analysis on land.

Dissolved Mn concentration determination
seaFAST and inductively coupled plasma mass spectrometry

The analysis for dissolved Mn was performed in the TracEx laboratory, University of Stellenbosch (South Africa), following the established method described by Samanta et al. (2021). The seaFAST and inductively coupled plasma mass spectrometry (ICP-MS) settings for sample runs are given in Supporting Information Tables ST2a, ST2b. Seawater samples were analyzed in duplicate bottles using an online SC-4 DX seaFAST S3 (ESI® seaFAST) preconcentration unit (X30) coupled with a quadrupole ICP-MS (Agilent® 7900). Briefly, 3 mL of seawater was taken up by the seaFAST unit, buffered with an ammonium acetate buffer to a pH of 6.0 ± 0.2, and loaded onto a high-affinity metal chelating resin column (Nobias EDTriA). Here, the metal ions, including Mn, were bound to the resin and separated from the seawater matrix elements, for example, Na, Mg, and Cl, which passed through the column. The metal ions were subsequently eluted in a 5% nitric acid (Ultrapur® HNO_3, Merck) from the resin column in low volumes (100 μL), resulting in a preconcentration factor of 30. On the ICP-MS, samples were introduced using a low self-aspirating perfluoroalkoxy nebulizer (PFA-ST microflow) with a flow rate of 0.4 mL min^{-1}. The accuracy of the
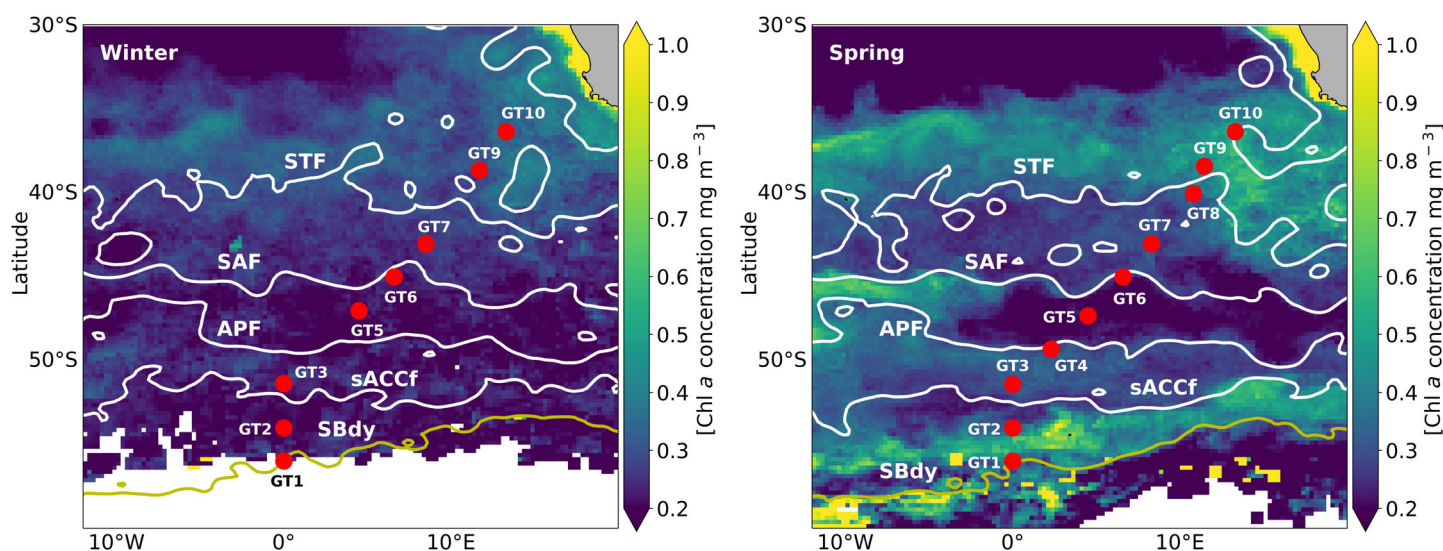
Fig. 2. Ocean color maps of the chlorophyll *a* (Chl *a*; mg m^{-3}) averaged for Winter (July and August) and Spring (October and November) in 2019, showing sampling stations during the SCALE winter and spring cruises between Cape Town, and the marginal ice zone in the South Atlantic sector of the Southern Ocean. The red dots indicate the stations sampled from south to north. The oceanic fronts are shown with abbreviations north to south; STF: Subtropical Front; SAF: Subantarctic Front; APF: Antarctic Polar Front; sACCf: Southern Antarctic Circumpolar Current Front; Sbdy: Southern Boundary. The positions of the fronts were determined by maps of absolute dynamic topography (ADT, m) from the Collecte Localisation Satellites-Archivage, Validation et Interprétation des données des Satellites Océanographiques (CLS-AVISO) product (Rio et al. 2011) using previously defined boundary definitions (Swart et al. 2010).

dissolved Mn analysis was quantified by comparing the analyzed values of NASS-7 certified reference materials and GEOTRACES GSC-19 (measured 2.17 ± 0.37 [*n* = 5]) and GSP-137 (measured 0.76 ± 0.13 [*n* = 5]) community reference materials which were compared with certified and consensus values respectively, in addition to quantification of in-house reference seawater (Supporting Information Table ST3). The laboratory-determined values were within the acceptable recovery range.

Blanks and limits of detection

The method blank was determined by analyzing 2% HCl (Ultrapur®; Merck). The limit of detection (LOD) was calculated as three times the standard deviation of the pre-concentrated blank (LOD = 0.01 nmol kg^{-1}; *n* = 13). The minimum dissolved Mn concentration observed in this study was 0.15 nmol kg^{-1}.

MLD dissolved Mn reservoir size

The MLD was defined using the density threshold criterion, as the depth where potential density differs from that of the surface (10 m) by more than 0.03 kg m^{-3} (de Boyer Montégut et al. 2004). The estimated seasonal reservoir sizes were calculated using the trapezoidal rule, by integrating the dissolved Mn concentrations from the surface (*z* = 0) to the base of the MLD (Eq. 1).

$$\text{Reservoir size}\left(\mu\text{mol}\,\text{m}^{-2}\right) = \int_{z=\text{MLD}_{\text{base}}}^{z=0} [\text{dMn}(z)]dz, \quad (1)$$

where *z* is depth (m) and dMn is dissolved Mn concentration (nmol kg^{-1}). Where there was no dissolved Mn observation directly at the MLD, a linear interpolation was performed between the nearest two points to estimate the concentration at that depth. Since the vertical sampling begins at a depth of 25 m, the concentration of dissolved Mn in surface waters (0 m) was taken as the same as 25 m. To eliminate bias caused by the MLD in the reservoir size calculation, we normalized the reservoir size by MLD and then compared it to the unnormalized reservoir size (as described in Eq. 1). The normalization was achieved by dividing the reservoir size by the MLD.

Calculations of dissolved Mn physical supply mechanisms to the mixed layer

Various physical fluxes to the mixed layer (except winter entrainment and spring detrainment) were calculated using two different methods: method 1 (daily integration) and method 2 (linear interpolation). Method 1 involved calculating physical fluxes for the winter occupation (μmol m^{-2} d^{-1}), where the obtained fluxes were multiplied by the difference in days between winter and spring occupations, yielding a dissolved Mn stock (μmol m^{-2}) representing the dissolved Mn available for phytoplankton uptake during the spring season. Method 2 assumed a linear daily change of dissolved Mn at the base of the MLD in the fluxes. Daily fluxes between winter and spring occupations were linearly interpolated, and the total fluxes were integrated over time (days). This integration

yielded a similar dMn stock (μmol m^{-2}) as method 1 for direct comparison.

Winter entrainment and spring detrainment

Winter entrainment, which involves the mixing of deeper water into the surface mixed layer, was estimated by integrating dissolved Mn from the surface (0 m) down to the maximum mixed layer (MLD$_{MAX}$) depth at each station (Eq. 1). MLD$_{MAX}$ was taken as the measured winter mixed layer during the winter cruise and in some cases (where the measured MLD was relatively shallow), as the maximum depth of mixing over the year. This was obtained from a monthly $1° \times 1°$ gridded data product EN4.2.2 (Good et al. 2013) of temperature and salinity profiles, which were used to estimate density, and then the de Boyer Montégut criterion was applied to calculate the MLD. This applied to stations GT1, GT3, and GT9. The winter-entrained dissolved Mn stock that is subsequently detrained during spring was estimated according to Eq. 2 (Tagliabue et al. 2014):

$$\text{Spring detrainment}(\mu\text{mol}\,\text{m}^{-2}) = \frac{\text{MLD}_{\text{Spring}}}{\text{MLD}_{\text{MAX}}} \times \text{Winter entrainment.} \quad (2)$$

Diapycnal diffusive flux

Total diapycnal diffusive flux estimates for the mixed layer were calculated for each sampled zone according to Eq. 3.

$$\text{Diapycnal diffusion}(\mu\text{mol}\,\text{m}^{-2}) = K_z \times \frac{\partial \text{dMn}}{\partial z_{\text{MLD}_{\text{base}}}} \times \text{time(d).} \quad (3)$$

where K_z is the vertical eddy diffusivity (10^{-3}, 10^{-4}, and 10^{-5} m^2 s^{-1}) (Cisewski et al. 2005) and $\partial\text{dMn}/\partial z_{\text{MLD}_{\text{base}}}$ is the vertical dissolved Mn gradient at the base of the MLD (μmol m^{-4}) (Tagliabue et al. 2014). Tagliabue et al. (2014) compared the three different K_z values to determine whether diapycnal diffusion can match biological utilization in the Southern Ocean when K_z approaches its lower and upper limits. Their findings suggest that with low K_z values, diapycnal diffusion is insufficient to match biological utilization estimates in half of the Southern Ocean. However, when K_z is at its highest, diapycnal diffusion can meet these biological needs in more than 50% of the Southern Ocean. In this study, the median value for the Southern Ocean of 10^{-4} m^2 s^{-1} (Cisewski et al. 2005) was used as a reference point for discussion.

Vertical Ekman pumping (upwelling and downwelling)

Ekman pumping, which represents the vertical movement of water driven by westerly winds, Coriolis force from Earth's rotation, and inertial forces (Morrison et al. 2015), was calculated by multiplying the surface northwards and eastwards component of the wind stress curl (kg m^{-1} s^{-2}) with the concentration of dissolved Mn at the base of the mixed layer. The wind stress components were obtained from the Copernicus

Climate Change Service (C3S) ERA5, which is the fifth generation of the European Centre for Medium-Range Weather Forecasts (ECMWF) atmospheric reanalysis of the global climate (Copernicus Climate Change Service, 2017). In the Southern Ocean, a positive wind stress curl indicates anticyclonic rotation, causing surface ocean convergence and resulting in downwelling. Conversely, a negative wind stress curl indicates cyclonic rotation, causing surface ocean divergence and leading to upwelling (McPhaden et al. 2008).

Equatorward lateral advection

Lateral dissolved Mn input, which refers to the horizontal transport of water and its preformed composition, was estimated by taking the latitudinal gradient in MLD dissolved Mn ($\partial\text{Mn}_{\text{MLD}}/\partial x$) with respect to the distance from the southernmost station (x), multiplied by the northward surface current velocity gradient with respect to x (m s^{-1}) and the MLD. The current velocity product was processed by Segment Sol Multimission Altimetry and Orbitography/Data Unification and Altimeter Combination System (SSALTO/DUACS) and distributed by AVISO+ (https://www.aviso.altimetry.fr) with support from Centre National d'Etudes Spatiales (CNES).

Remote sensing chlorophyll *a*

Chlorophyll *a* data were obtained from the Ocean Color Climate Change Initiative v6.0 product (Sathyendranath et al. 2019).

Results

Study area hydrography

From north to south, the sampled zones were the subtropical zone (STZ; $34.60 <$ practical salinity (S) < 35.50, potential temperature (θ) $\geq 17.9°$C), subantarctic zone (SAZ; $34.21 < S < 34.81$, $5°$C$< \theta < 11°$C), polar frontal zone (PFZ; $34.03 < S < 34.78$, $2°$C$< \theta < 6°$C), and the antarctic zone (AAZ; $33.85 < S < 34.74$, $\theta < 2°$C). During the winter season, the MLDs were comparatively deeper, 131 ± 41 m (mean $\pm$ standard deviation), than in spring, 57 ± 31 m (Supporting Information Table ST4), and the MLD reservoir sizes showed decreases from winter, $65.21 \pm 12.93\,\mu$mol m^{-2}, to spring, $21.64 \pm 19.32\,\mu$mol m^{-2}, in all the stations as the mixed layers shoaled.

Seasonal dissolved Mn concentration in the upper 500 m of the water column

During winter (Fig. 3a), the vertical profiles in the STZ and SAZ showed elevated surface concentrations, followed by subsurface maxima at 100 m, before decreasing with depth in the rest of the upper water column (< 500 m). Comparatively, PFZ and AAZ showed similar surface concentration elevations as described for STZ and SAZ but with subsurface maxima at ~ 250 m before decreasing below 250 m. Winter concentrations in the upper water column ranged from 0.15 to 0.84 nmol kg^{-1}, whereas in spring (0.18–1.17 nmol kg^{-1}), dissolved Mn concentrations displayed consistent scavenged-like
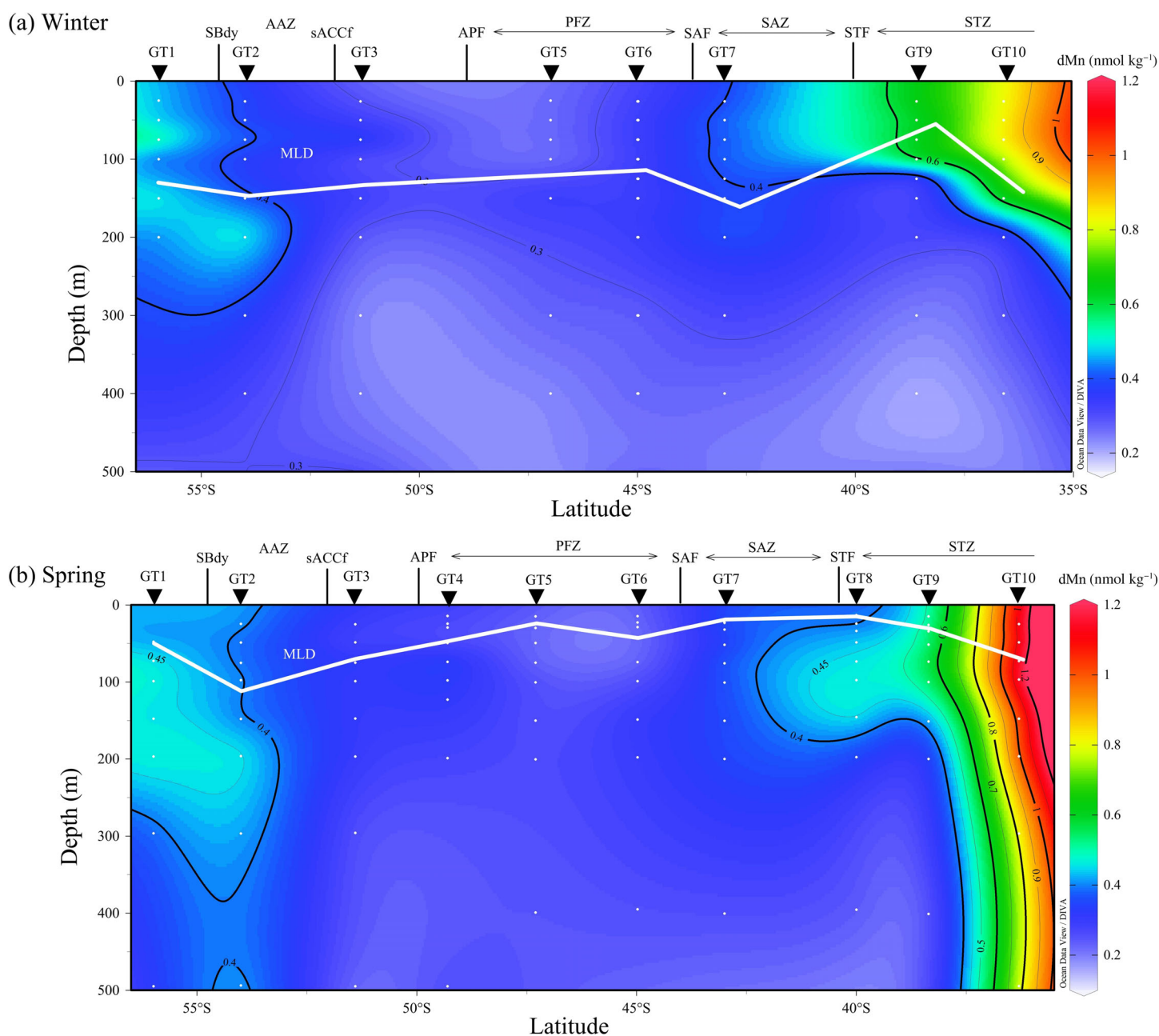
Fig. 3. Distribution of dissolved manganese (dMn; nmol kg^{-1}) for the upper 500 m in (**a**) winter and (**b**) spring. The white dots represent the sampling depths throughout the water column. The colorbar shows dMn concentration (nmol kg^{-1}). The white horizontal lines show the seasonal MLD. The figure was produced using Ocean Data View (Schlitzer 2018, https://odv.awi.de, 2018).

profiles (Fig. 3b; Supporting Information Figure SF1). These were characterized by elevated concentrations between 0 and 100 m (0.42 ± 0.24 nmol kg^{-1}), increasing to maximum concentration up to 1.17 nmol kg^{-1} between 100 and 300 m before decreasing to relatively low values (0.33 ± 0.17 nmol kg^{-1}) at depths greater than 300 m. In winter, there is evidence of deep-water dissolved Mn maxima at stations GT2 (0.55 nmol kg^{-1}) and GT7 (0.65 nmol kg^{-1}) at ~ 1200 m (Supporting Information Figure SF1), with no evidence of the same deep-water maxima in spring. Mean winter dissolved Mn

concentrations (0.32 ± 0.08 nmol kg^{-1}) were comparable with spring (0.34 ± 0.19 nmol kg^{-1}) in the upper 500 m, with no evidence of significant differences ($p > 0.05$; Student's t-test).

Discussion

Comparison with previously reported dissolved Mn distributions in the Southern Ocean

This study addresses a research gap in understanding the spatial and temporal variability of Mn cycling by presenting

the first winter dissolved Mn measurements along the zero meridian (0°E) in the Atlantic sector of the Southern Ocean. Our dissolved Mn concentrations had similar ranges of 0.15–0.84 and 0.18–1.17 nmol kg^{-1} in winter and spring, respectively, for the upper 500 m of the water column. The profiles generally showed surface elevation and subsurface maxima in the remineralization depth range before decreasing with depth. Interestingly, the presence of a second dissolved Mn maximum below the remineralization depth range at stations GT2 and GT7 could possibly be linked to slower remineralization and dissolution rates of the refractory phase of particulate Mn. When compared to other dissolved Mn measurements in the Southern Ocean, our data exhibited consistency with previously reported concentration ranges, which were predominantly conducted during summer and autumn (Fig. 4). For instance, dissolved Mn observations from the BONUS-GoodHope cruise in summer ranged from 0.21 to 1.30 nmol kg^{-1} (Boye et al. 2012), which are comparable to our spring data (0.18–1.17 nmol kg^{-1}). Whilst a second

study on the zero meridian line in summer had dissolved Mn concentrations that were comparatively lower than our spring values, ranging from 0.04 to 0.64 nmol kg^{-1} in the top 500 m of the water column (Middag et al. 2011a). These differences may possibly be because their sampling occurred toward the end of the productive season, approaching autumn where most of the dissolved Mn would have been biologically utilized during the spring and summer growth seasons. In the rest of the Southern Ocean, surface concentrations were slightly lower than our spring Mn ranges. For example, concentrations ranging from 0.10 to 0.25 nmol kg^{-1} in the top 500 m are reported in the Drake Passage during autumn (Middag et al. 2012), and 0.15–0.21 nmol kg^{-1} in the top 500 m of Weddell Sea during the end of summer (Middag et al. 2013). In this study, a slight localized increase in dissolved Mn concentration (0.40–0.45 nmol kg^{-1}) is observed in the deeper layer > 1500 m, particularly at shallow bathymetry stations, for example, above the mid-ocean ridge at station GT2 in the AAZ (Supporting Information Figure SF1). This
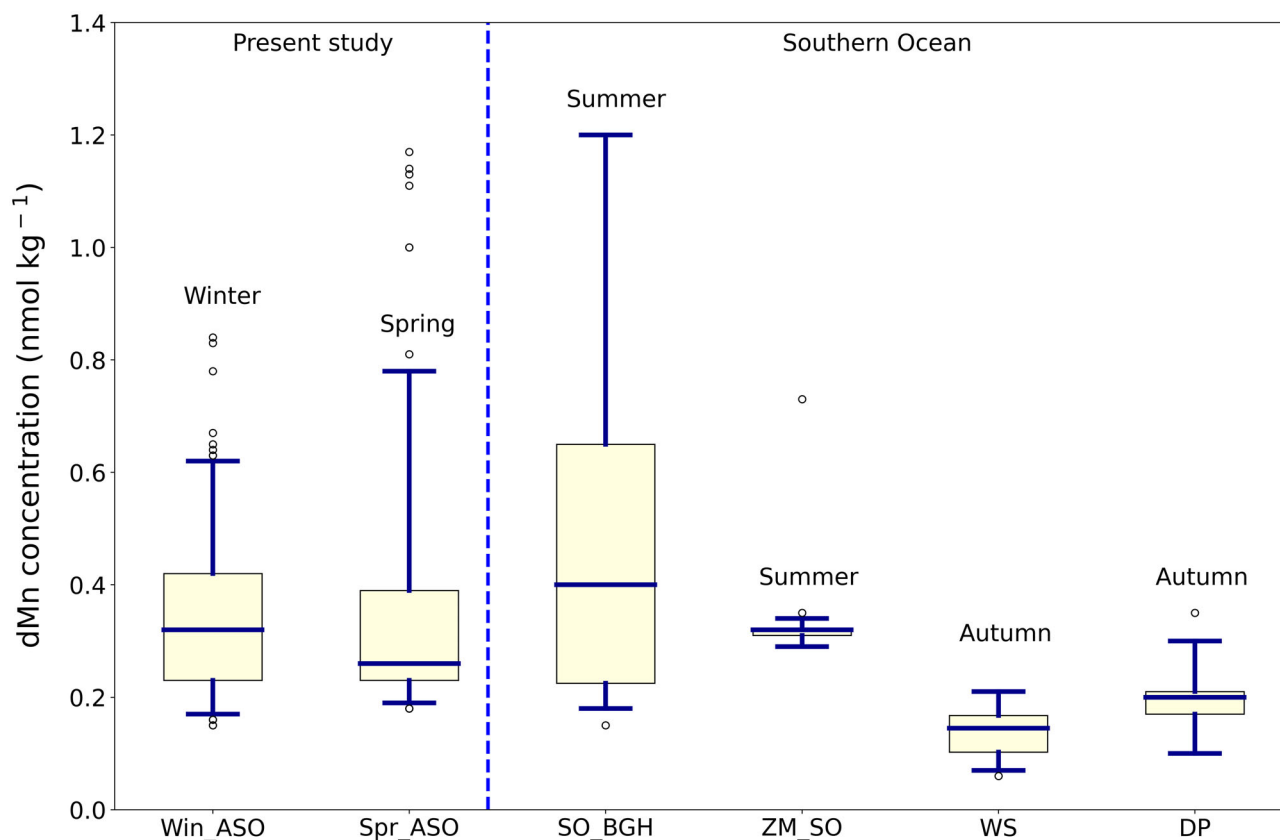

Fig. 4. Comparative box and whisker plots of dissolved Mn (dMn; nmol kg^{-1}) for full-depth profiles. Data compiled from all available data from the GEOTRACES intermediate data product 2021v2 (GEOTRACES Intermediate Data Product Group 2023). The boxplots show the median (horizontal line inside the box), the box shows the interquartile range (first to the third quartile), and the whiskers show the 5th–95th percentile of the data. Beyond this, the circles represent outliers. The *x*-axis abbreviations and references from left to right are as follows: Win_ASO (Winter Atlantic Southern Ocean—this study, *n* = 134), Spr_ASO (Spring Atlantic Southern Ocean—this study, *n* = 145), SO_BGH (Southern Ocean summer BONUS-GoodHope, *n* = 233; Boye et al. 2012), ZM_SO (zero meridian Southern Ocean summer, *n* = 468; Middag et al. 2011a), WS (Weddell Sea end of summer, *n* = 176; Middag et al. 2013), and DP (Drake Passage autumn, *n* = 221; Middag et al. 2012).
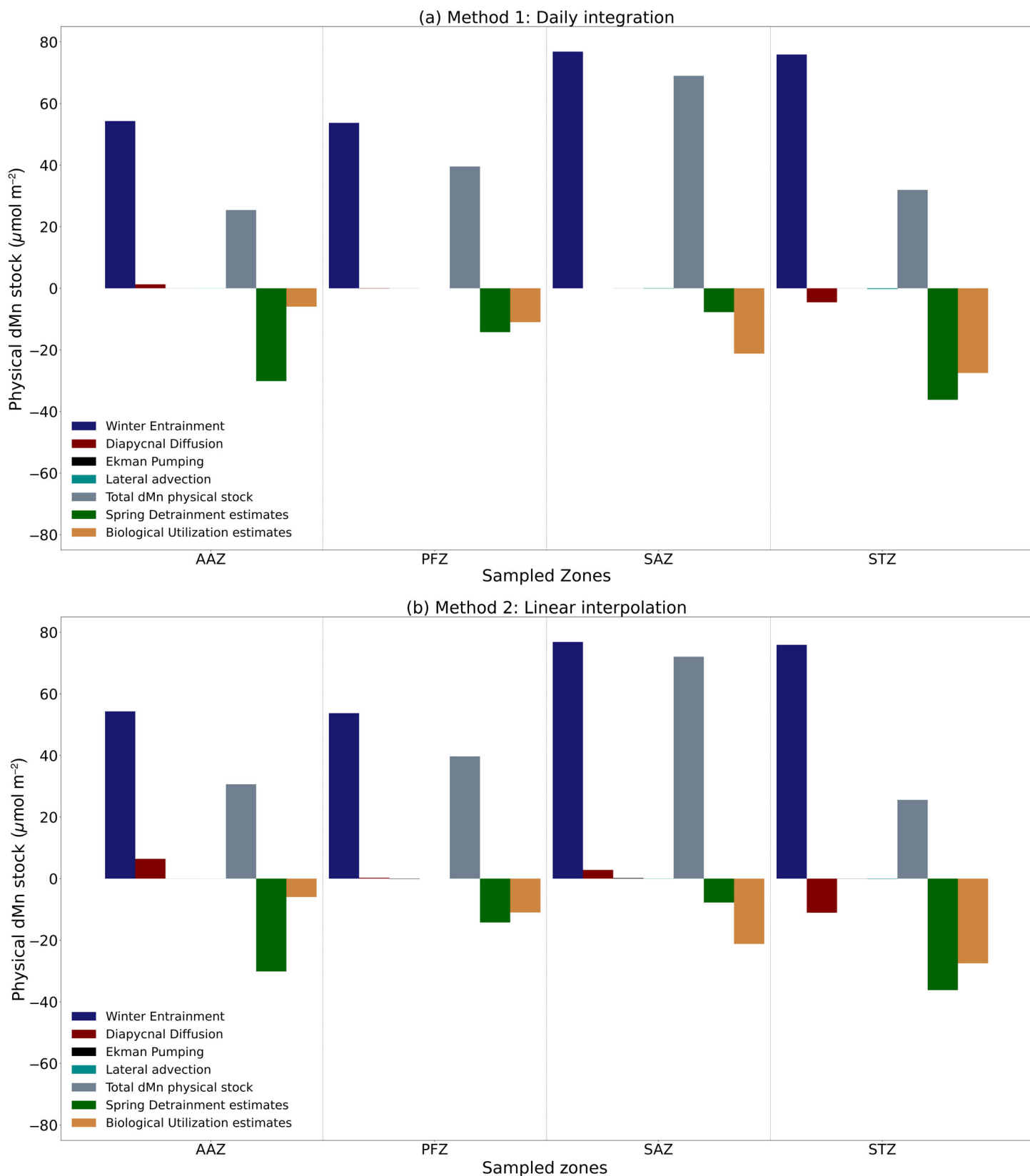
(Figure legend continues on next page.)

observed increase is likely due to hydrothermal inputs, indicating a potential source of dissolved Mn in this region, as shown by previous studies (Middag et al. 2011a). However, our study found no evidence of this source being advected into the mixed layer.

Winter dissolved Mn physical fluxes to the mixed layer

We estimated various physical mechanisms, including winter entrainment, diapycnal diffusion, vertical Ekman pumping, and lateral advection, which transport dissolved Mn between the subsurface and surface mixed layer. The relative magnitudes of fluxes for the different transport processes varied along the sampled zones (Fig. 5; Supporting Information Tables ST5a, ST5b), but winter entrainment and diapycnal diffusion seem to be the dominant processes affecting the flux. Winter entrainment varied from 54.31 μmol m^{-2} in the AAZ to a peak of 76.86 μmol m^{-2} in the SAZ, contributing 89.33–99.99% of the total flux with moderate variability (97.23% $\pm$ 5.28%). Whereas diapycnal diffusive flux ranged from -11.06 μmol m^{-2} in the STZ to 6.43 μmol m^{-2} in the AAZ, contributing 0.52–10.58% of the total flux (4.92% $\pm$ 5.14%) into the mixed layer, when using a typical vertical eddy diffusivity constant of 10^{-4} m^2 s^{-1} for the Southern Ocean. The negative value for diapycnal diffusive flux in the STZ indicates that the diffusive process acts as a sink, removing 14.56% dissolved Mn from the mixed layer in this region. This happens because there is a negative concentration gradient with depth caused by higher dissolved Mn concentrations at the surface compared to the subsurface, possibly from the Indian Ocean via the Agulhas current leakage (as in the case of the trace metal lead; Samanta et al. 2023). Lateral advection acted as a weak flux of dissolved Mn to the mixed layer across all zones, contributing an average of 0.10% $\pm$ 0.06% to the total flux. Vertical Ekman pumping fluxes were similarly small, ranging from -7.76×10^{-3} μmol m^{-2} in the AAZ to 2.70×10^{-2} μmol m^{-2} in the PFZ, contributing 0.01% $\pm$ 0.04% of the total flux. Notably, downwelling (negative Ekman pumping) occurred in the AAZ and SAZ. The highest to lowest cumulative fluxes calculated for winter using method 1, obtained by summing the individual fluxes, were as follows: 69.00 μmol m^{-2} in the SAZ, 39.46 μmol m^{-2} in the PFZ, 31.95 μmol m^{-2} in the STZ, and 25.49 μmol m^{-2} in the AAZ (Fig. 5a; Supporting Information Table ST5a). Using method 2, the highest to lowest cumulative fluxes were as follows: 72.08 μmol m^{-2} in the SAZ, 39.70 μmol m^{-2} in the PFZ, 30.65 μmol m^{-2} in the AAZ, and 25.57 μmol m^{-2} in the STZ

(Fig. 5b; Supporting Information Table ST5b), showing insignificant variation between both methods ($p > 0.05$; Student's t-test). In spring, estimates for detrainment, serving as a dissolved Mn sink, ranged from a maximum of -36.21 μmol m^{-2} in the STZ to a minimum of -7.75 μmol m^{-2} in the SAZ. It is important to note that the impact of scavenging and other loss factors on this stock is recognized, although these effects were not quantified in the current study.

Primary production and dissolved Mn utilization in the Atlantic sector of the Southern Ocean

Here, we examine if the total calculated dissolved Mn fluxes to the mixed layer can meet estimates of biological dissolved Mn consumption (i.e., do regions of higher dissolved Mn fluxes have higher Mn utilization and higher net primary production). This was done using the net primary production estimates from the CAFE model (Silsbe et al. 2016) applied to the Ocean Color Climate Change Initiative remote sensing data (Ryan-Keogh et al. 2023) and a median Mn : carbon ratio of 3 μmol Mn : mol carbon (Hawco et al. 2022). Net primary production estimates ranged from 291.96 to 1729.54 mg C m^{-2} d^{-1} (800.13 $\pm$ 506.45 mg C m^{-2} d^{-1}) in the sampled region, increasing northwards along the transect, reaching maximum values near the continental margins in the STZ. Based on the net primary production estimates and the Mn : carbon ratio, dissolved Mn utilization integrated per day between winter and spring increased northwards, ranging from 5.96 $\pm$ 0.14 μmol m^{-2} in the AAZ, 10.99 $\pm$ 0.10 μmol m^{-2} in the PFZ, 21.20 $\pm$ 1.47 μmol m^{-2} in the SAZ and 27.51 $\pm$ 2.02 μmol m^{-2} in the STZ (Fig. 5). When comparing these Mn utilization rates with the calculated total dissolved Mn supply (see Winter dissolved Mn physical fluxes to the mixed layer), it was found that in the STZ, the Mn utilization rates were greater than the supply. This indicated that the total dissolved Mn supply was not enough to meet biological demands in the STZ, offset by the large diapycnal diffusive sink of -11.06 μmol m^{-2} and larger detrainment term. While phytoplankton typically rely on internal recycling and remineralization of particulate Mn to meet their biological demands, we couldn't correctly quantify this source in our study due to unreliable oxygen sensor data obtained during the cruise. To account for phytoplankton community structure influencing the dissolved Mn utilization, we performed a sensitivity analysis by using Mn : carbon ratios ranging from 1 to 10 μmol : mol (Hawco et al. 2022; Sofen et al. 2022). The utilization rates were still less than the total dissolved Mn physical supply in the Southern

(Figure legend continued from previous page.)
Fig. 5. Winter physical fluxes to the mixed layer (μmol m^{-2} d^{-1}), integrated per day between winter and spring using (**a**) method 1 (integrated by days between occupations) and (**b**) method 2 (linearly interpolated between occupations) to give stock/reservoir size (μmol m^{-2}) showing winter entrainment stock (μmol m^{-2}), diapycnal diffusion stock (μmol m^{-2}), Ekman transport (μmol m^{-2}), lateral advection (μmol m^{-2}), total physically mediated dissolved Mn (dMn) stock (μmol m^{-2}) springtime detrainment estimates of dMn removed from the mixed layer (μmol m^{-2}), and estimates of biological utilization (μmol m^{-2}).

Ocean portion of the transect, while in the STZ, the utilization rates were still greater than the physical dissolved Mn supply. This suggests that in the STZ, there might be a missing (unaccounted) dissolved Mn supply mechanism to match the biological demands. However, it is also important to consider any error in the net primary production estimates that will be contributing to this mismatch in supply and biological demand.

Potential sources of Mn in the STZ could include continental sources and possibly the input from the Indian Ocean water through the Agulhas current leakage, which suggests the significance of the Agulhas Current in potentially co-regulating net primary production in the South Atlantic sector of the Southern Ocean. Other missing physical mechanisms could include coastal upwelling, mesoscale eddies, horizontal diffusion, wind-driven entrainment, and isopycnal mixing. However, errors in the calculation of the physical fluxes cannot be discounted. For example, when we consider the calculation of diapycnal diffusion, which is influenced by variable K_z values. If we apply a greater vertical eddy diffusivity constant of 10^{-3} m^2 s^{-1}, we find that the contribution of the diapycnal diffusion to the total dissolved Mn flux in the South Atlantic is $13.28\% \pm 2.86\%$. However, if we apply the lower range constant (10^{-5} m^2 s^{-1}), the average diapycnal flux drops to $0.40\% \pm 0.23\%$. Regardless of this variable eddy diffusivity, the estimated STZ supply mechanisms are insufficient to match estimated biological demands.

Conclusions

This study examined the role of winter-dissolved Mn stock as a source of the spring mixed layer, which is then potentially available for biological consumption. The observed dissolved Mn concentrations in winter and spring were in the nanomolar scale, averaging 0.32 ± 0.08 and 0.34 ± 0.19 nmol kg^{-1}, respectively. The primary fluxes of dissolved Mn to the mixed layer are the winter entrainment pulse ($97.23\% \pm 5.28\%$ of total physical dissolved Mn supply), followed by diapycnal diffusion ($4.92\% \pm 5.14\%$ of total physical dissolved Mn supply). This resulted in mean reservoir sizes in winter and spring of 65.21 ± 12.93 and 21.64 ± 19.32 μmol m^{-2}, respectively, with dissolved Mn losses between the two seasons averaging 43.57 ± 19.57 μmol m^{-2} showing high variability between biogeochemical zones. The total dissolved Mn supplied through winter entrainment and diapycnal diffusion to the STZ was not enough to match phytoplankton utilization demands, suggesting some evidence of other physical supply mechanisms in this region that need to be quantified. However, in the SAZ, PFZ, and AAZ, the physical fluxes of dissolved Mn were able to satisfy phytoplankton biological demand estimates. Nevertheless, diapycnal diffusion, vertical Ekman upwelling, lateral advection, and storm-driven entrainment can still contribute to the reservoir sizes year-round after the winter entrainment pulse.

Data availability statement

References

Anugerahanti, P., and A. Tagliabue. 2023. Process controlling iron-manganese regulation of the Southern Ocean biological carbon pump. Philos. Trans. A Math. Phys. Eng. Sci. **381**: 20220065. doi:10.1098/rsta.2022.0065

Ardyna, M., and others. 2019. Hydrothermal vents trigger massive phytoplankton blooms in the Southern Ocean. Nat. Commun. **10**: 2451. doi:10.1038/s41467-019-09973-6

Balaguer, J., F. Koch, C. Hassler, and S. Trimborn. 2022. Iron and manganese co-limit the growth of two phytoplankton groups dominant at two locations of the Drake Passage. Commun. Biol. **5**: 207. doi:10.1038/s42003-022-03148-8

Boyd, P. W., and others. 2000. A mesoscale phytoplankton bloom in the polar Southern Ocean stimulated by iron fertilization. Nature **407**: 695–702. doi:10.1038/35037500

Boye, M., B. D. Wake, P. L. Garcia, J. Bown, A. R. Baker, and E. P. Achterberg. 2012. Distributions of dissolved trace metals (Cd, Cu, Mn, Pb, Ag) in the southeastern Atlantic and the Southern Ocean. Biogeosciences **9**: 3231–3246. doi:10.5194/bg-9-3231-2012

Bristow, L. A., W. Mohr, S. Ahmerkamp, and M. M. M. Kuypers. 2017. Nutrients that limit growth in the ocean. Curr. Biol. **27**: R474–R478. doi:10.1016/j.cub.2017.03.030

Bucciarelli, E., S. Blain, and P. Tréguer. 2001. Iron and manganese in the wake of the Kerguelen Islands (Southern Ocean). Mar. Chem. **73**: 21–36. doi:10.1016/S0304-4203(00)00070-0

Cisewski, B., V. H. Strass, and H. Prandke. 2005. Upper-ocean vertical mixing in the Antarctic Polar Front Zone. Deep-Sea Res. II: Top. Stud. Oceanogr. **52**: 1087–1108. doi:10.1016/j.dsr2.2005.01.010

Cloete, R., J. C. Loock, N. R. van Horsten, S. Fietz, T. N. Mtshali, H. Planquette, and A. N. Roychoudhury. 2021. Winter biogeochemical cycling of dissolved and particulate cadmium in the Indian sector of the Southern Ocean (GEOTRACES GIpr07 transect). Front. Mar. Sci. **8**: 656321. doi:10.3389/fmars.2021.656321

Cutter, G. A., K. Casciotti, P. L. Croot, W. Geibert, L.-E. Heimbürger, M. Lohan, H. Planquette, and T. van de Flierdt. 2017. Sampling and sample-handling protocols for GEOTRACES cruises. Version 3, August 2017. GEOTRACES Community Practices. http://www.geotraces.org/images/stories/documents/intercalibration/Cookbook.pdf

de Boyer Montégut, C., G. Madec, A. S. Fischer, A. Lazar, and D. Iudicone. 2004. Mixed layer depth over the global ocean: An examination of profile data and a profile-based climatology. J. Geophys. Res. **109**: C12003. doi:10.1029/2004JC002378

de Jong, J., V. Schoemann, D. Lannuzel, P. Croot, H. de Baar, and J. L. Tison. 2012. Natural iron fertilization of the Atlantic sector of the Southern Ocean by continental shelf sources of the Antarctic Peninsula. J. Geophys. Res. **117**: G01029. doi:10.1029/2011JG001679

GEOTRACES Intermediate Data Product Group. 2023. The GEOTRACES intermediate data product 2021v2 (IDP2021v2). NERC EDS British Oceanographic Data Centre NOC. doi:10.5285/ff46f034-f47c-05f9-e053-6c86abc0dc7e

Good, S. A., M. J. Martin, and N. A. Rayner. 2013. EN4: Quality controlled ocean temperature and salinity profiles and monthly objective analyses with uncertainty estimates. J. Geophys. Res.: Oceans **118**: 6704–6716. doi:10.1002/2013JC009067

Hawco, N. J., A. Tagliabue, B. S. Twining, and N. Hawco. 2022. Manganese limitation of phytoplankton physiology and productivity in the Southern Ocean. Glob. Biogeochem. Cycles **36**: e2022GB007382. doi:10.1029/2022GB007382

Laglera, L. M., and others. 2017. Iron partitioning during LOHAFEX: Copepod grazing as a major driver for iron recycling in the Southern Ocean. Mar. Chem. **196**: 148–161. doi:10.1016/j.marchem.2017.08.011

Latour, P., and others. 2021. Manganese biogeochemistry in the Southern Ocean, from Tasmania to Antarctica. Limnol. Oceanogr. **66**: 2547–2562. doi:10.1002/lno.11772

McPhaden, M. J., M. F. Cronin, and D. C. McClurg. 2008. Meridional structure of the seasonally varying mixed layer temperature balance in the eastern tropical Pacific. J. Clim. **21**: 3240–3260. doi:10.1175/2007JCLI2115.1

Mendez, J., C. Guieu, and J. Adkins. 2010. Atmospheric input of manganese and iron to the ocean: Seawater dissolution experiments with Saharan and North American dusts. Mar. Chem. **120**: 34–43. doi:10.1016/j.marchem.2008.08.006

Middag, R., H. J. W. de Baar, P. Laan, P. H. Cai, and J. C. van Ooijen. 2011a. Dissolved manganese in the Atlantic sector of the Southern Ocean. Deep-Sea Res. II: Top. Stud. Oceanogr. **58**: 2661–2677. doi:10.1016/j.dsr2.2010.10.043

Middag, R., H. J. W. de Baar, P. Laan, and M. B. Klunder. 2011b. Fluvial and hydrothermal input of manganese into the Arctic Ocean. Geochim. Cosmochim. Acta **75**: 2393–2408. doi:10.1016/j.gca.2011.02.011

Middag, R., H. J. W. de Baar, P. Laan, and O. Huhn. 2012. The effects of continental margins and water mass circulation on the distribution of dissolved aluminum and manganese in Drake Passage. J. Geophys. Res. **117**: C01019. doi:10.1029/2011JC007434

Middag, R., H. J. W. de Baar, M. B. Klunder, and P. Laan. 2013. Fluxes of dissolved aluminum and manganese to the Weddell Sea and indications for manganese co-limitation. Limnol. Oceanogr. **58**: 287–300. doi:10.4319/lo.2013.58.1.0287

Morrison, A. K., T. L. Frölicher, and J. L. Sarmiento. 2015. Upwelling in the Southern Ocean. Phys. Today **68**: 27–32. doi:10.1063/PT.3.2654

Oldham, V. E. 2017. The complexation chemistry of dissolved manganese(III) in the ocean and its role in the coupled cycles of carbon, iron and sulfur. Doctoral dissertation. Univ. of Delaware. https://udspace.udel.edu/handle/19716/21735#files-area

Peers, G., and N. M. Price. 2004. A role for manganese in superoxide dismutases and growth of iron-deficient diatoms. Limnol. Oceanogr. **49**: 1774–1783. doi:10.4319/lo.2004.49.5.1774

Raven, J. A. 1990. Predictions of Mn and Fe use efficiencies of phototrophic growth as a function of light availability for growth and of C assimilation pathway. New Phytol. **116**: 1–18. doi:10.1111/j.1469-8137.1990.tb00505.x

Richon, C., and A. Tagliabue. 2021. Biogeochemical feedbacks associated with the response of micronutrient recycling by zooplankton to climate change. Glob. Change Biol. **27**: 4758–4770. doi:10.1111/gcb.15789

Rigby, S. J., R. G. Williams, E. P. Achterberg, and A. Tagliabue. 2020. Resource availability and entrainment are driven by offsets between nutriclines and winter mixed-layer depth. Glob. Biogeochem. Cycles **34**: e2019GB006497. doi:10.1029/2019GB006497

Rio, M. H., S. Guinehut, and G. Larnicol. 2011. New CNES-CLS09 global mean dynamic topography computed from the combination of GRACE data, altimetry, and in situ measurements. J. Geophys. Res. **116**: C07018. doi:10.1029/2010JC006505

Ryan-Keogh, T. J., S. J. Thomalla, N. Chang, and T. Moalusi. 2023. A new global oceanic multi-model net primary productivity data product. Earth Syst. Sci. Data **2**: 4829–4848. doi:10.5194/essd-15-4829-2023

Sallée, J. B., and others. 2021. Summertime increases in upper-ocean stratification and mixed-layer depth. Nature **591**: 592–598. doi:10.1038/s41586-021-03303-x

Samanta, S., R. Cloete, J. Loock, R. Rossouw, and A. N. Roychoudhury. 2021. Determination of trace metal (Mn, Fe, Ni, Cu, Zn, Co, Cd and Pb) concentrations in seawater using single quadrupole ICP-MS: A comparison between offline and online preconcentration setups. Minerals **11**: 1289. doi:10.3390/min11111289

Samanta, S., and others. 2023. Exchange of Pb from Indian to Atlantic Ocean is driven by Agulhas current and atmospheric Pb input from South Africa. Sci. Rep. **13**: 5465. doi:10.1038/s41598-023-32613-5

Sander, S. G., and A. Koschinsky. 2011. Metal flux from hydrothermal vents increased by organic complexation. Nat. Geosci. **4**: 145–150. doi:10.1038/ngeo1088

Sathyendranath, S., and others. 2019. An ocean-colour time series for use in climate studies: The experience of the ocean-colour climate change initiative (OC-CCI). Sensors **19**: 4285. doi:10.3390/s19194285

Schlitzer, R. 2002. Carbon export fluxes in the Southern Ocean: Results from inverse modeling and comparison with satellite-based estimates. Deep-Sea Res. II: Top. Stud. Oceanogr. **49**: 1623–1644. doi:10.1016/S0967-0645(02)00004-8

Schlitzer, R. 2018. Ocean data view. https://odv.awi.de

Silsbe, G. M., M. J. Behrenfeld, K. H. Halsey, A. J. Milligan, and T. K. Westberry. 2016. The CAFE model: A net production model for global ocean phytoplankton. Glob. Biogeochem. Cycles **30**: 1756–1777. doi:10.1002/2016GB005521

Sofen, L. E., and others. 2022. Trace metal contents of autotrophic flagellates from contrasting open-ocean ecosystems. Limnol. Oceanogr.: Lett. **7**: 354–362. doi:10.1002/lol2.10258

Sunda, W. G., and S. A. Huntsman. 1988. Effect of sunlight on redox cycles of manganese in the southwestern Sargasso Sea. Deep-Sea Res. I: Oceanogr. Res. Pap. **35**: 1297–1317. doi:10.1016/0198-0149(88)90084-2

Sunda, W. G., and S. A. Huntsman. 1994. Photoreduction of manganese oxides in seawater. Mar. Chem. **46**: 133–152. doi:10.1016/0304-4203(94)90051-5

Sunda, W. G., and S. A. Huntsman. 1998. Interactive effects of external manganese, the toxic metals copper and zinc, and light in controlling cellular manganese and growth in a coastal diatom. Limnol. Oceanogr. **43**: 1467–1475. doi:10.4319/lo.1998.43.7.1467

Sverdrup, H. U. 1953. On conditions for the vernal blooming of phytoplankton. ICES J. Mar. Sci. **18**: 287–295. doi:10.1093/icesjms/18.3.287

Swart, S., S. Speich, I. J. Ansorge, and J. R. E. Lutjeharms. 2010. An altimetry-based gravest empirical mode south of Africa: 1. Development and validation. J. Geophys. Res. **115**: C03002. doi:10.1029/2009JC005299

Tagliabue, A., T. Mtshali, O. Aumont, A. R. Bowie, M. B. Klunder, A. N. Roychoudhury, and S. Swart. 2012. A global compilation of dissolved iron measurements: Focus on distributions and processes in the Southern Ocean. Biogeosciences **9**: 2333–2349. doi:10.5194/bg-9-2333-2012

Tagliabue, A., J. B. Sallée, A. R. Bowie, M. Lévy, S. Swart, and P. W. Boyd. 2014. Surface-water iron supplies in the Southern Ocean sustained by deep winter mixing. Nat. Geosci. **7**: 314–320. doi:10.1038/ngeo2101

Tebo, B. M. L. 2019. Manganese cycling in the oceans. *In* Encyclopedia of water: Science, technology, and society. John Wiley & Sons. doi:10.1002/9781119300762.wsts0065

Twining, B. S., and S. B. Baines. 2013. The trace metal composition of marine phytoplankton. Ann. Rev. Mar. Sci. **5**: 191–215. doi:10.1146/annurev-marine-121211-172322

van Hulten, M., R. Middag, J. C. Dutay, H. de Baar, M. Roy-Barman, M. Gehlen, A. Tagliabue, and A. Sterl. 2017. Manganese in the west Atlantic Ocean in the context of the first global ocean circulation model of manganese. Biogeosciences **14**: 1123–1152. doi:10.5194/bg-14-1123-2017

Wedepohl, K. H. 1995. The composition of the continental crust. Geochim. Cosmochim. Acta **59**: 1217–1232. doi:10.1016/0016-7037(95)00038-2

Acknowledgments

Conflict of Interest

None declared.